FULL PAPER

Thin-Film Solar Cells with InP Absorber Layers Directly Grown on Nonepitaxial Metal Substrates

Maxwell Zheng, Hsin-Ping Wang, Carolin M. Sutter-Fella, Corsin Battaglia, Shaul Aloni, Xufeng Wang, James Moore, Jeffrey W. Beeman, Mark Hettick, Matin Amani, Wei-Tse Hsu, Joel W. Ager, Peter Bermel, Mark Lundstrom, Jr-Hau He, and Ali Javey*

The design and performance of solar cells based on InP grown by the nonepitaxial thin-film vapor–liquid–solid (TF-VLS) growth technique is investigated. The cell structure consists of a Mo back contact, p-InP absorber layer, n-TiO$_2$ electron selective contact, and indium tin oxide transparent top electrode. An ex situ p-doping process for TF-VLS grown InP is introduced. Properties of the cells such as optoelectronic uniformity and electrical behavior of grain boundaries are examined. The power conversion efficiency of first generation cells reaches 12.1% under simulated 1 sun illumination with open-circuit voltage (V_{OC}) of 692 mV, short-circuit current (J_{SC}) of 26.9 mA cm^{-2}, and fill factor (FF) of 65%. The FF of the cell is limited by the series resistances in the device, including the top contact, which can be mitigated in the future through device optimization. The highest measured V_{OC} under 1 sun is 692 mV, which approaches the optically implied V_{OC} of ≈795 mV extracted from the luminescence yield of p-InP.

1. Introduction

In recent years, the photovoltaic market has grown significantly as module prices have continued to come down. Continued growth of the field requires higher efficiency modules at lower manufacturing costs. In particular, higher power conversion efficiencies reduce the area needed for a given power output, thus reducing the downstream balance of systems costs that scale with area such as mounting frames, installation, and soft costs. While photovoltaic (PV) devices based on III–V absorbers have the highest reported efficiencies,[1] the manufacturing is still complex and costly.[2,3] There is a need for new materials growth, processing and fabrication techniques to address this major shortcoming of III–V-based photovoltaics. Significant progress on this front has been made by the epitaxial lift-off and transfer technique developed for gallium arsenide (GaAs),[1,4,5] which allows for limited reuse of costly epitaxial substrates.

Here we present an alternative approach using indium phosphide (InP) thin films grown directly on metal substrates. InP has a direct band gap of 1.344 eV, which is optimal for maximum efficiency in single junction solar cells.[6] Recently we developed the thin-film vapor–liquid–solid (TF-VLS) growth technique to produce high optoelectronic quality InP absorber layers directly on molybdenum (Mo) substrates. In this implementation of the technique, a layer of indium (In) confined between a Mo substrate and a silica (SiO$_x$) cap is heated to a temperature at which In is a liquid. The SiO$_x$ cap serves to prevent In evaporation and dewetting of the liquid In. Then, phosphorus vapor is introduced which diffuses through the SiO$_x$ cap into the In liquid, causing precipitation of solid InP. The InP grows into a polycrystalline film with ultra-large (>100 µm) lateral grain sizes.[7,8] This templated process extends the use of VLS for growth of structures beyond nanowires.[9–11] The

Dr. M. Zheng, H.-P. Wang, Dr. C. M. Sutter-Fella,
Dr. C. Battaglia, M. Hettick, M. Amani,
Dr. W.-T. Hsu, Prof. A. Javey
Electrical Engineering and Computer
Sciences Department
University of California
Berkeley, CA 94720, USA
E-mail: ajavey@berkeley.edu
Dr. M. Zheng, H.-P. Wang, Dr. C. M. Sutter-Fella,
Dr. C. Battaglia, J. W. Beeman, M. Hettick, M. Amani,
Dr. W.-T. Hsu, Dr. J. W. Ager, Prof. A. Javey
Materials Sciences Division
Lawrence Berkeley National Laboratory
Berkeley, CA 94720, USA

Dr. S. Aloni
Molecular Foundry
Lawrence Berkeley National Laboratory
Berkeley, CA 94720, USA
Dr. X. Wang, J. Moore, Prof. P. Bermel,
Prof. M. Lundstrom
School of Electrical and Computer Engineering
Purdue University
West Lafayette, IN 47907, USA
Prof. J.-H. He
Computer Electrical and Mathematical Sciences &
Engineering Division
King Abdullah University of Science and Technology
Thuwal 23955, Saudi Arabia

ADVANCED
ENERGY
MATERIALS

www.advenergymat.de

Materials
Views

www.MaterialsViews.com

benefits of TF-VLS growth over traditional vapor–solid (VS) growth methods, such as metalorganic chemical vapor deposition (MOCVD), are high throughput, high materials utilization efficiency and most importantly, the ability to obtain significantly larger (>100×) lateral grain sizes, and thus higher optoelectronic quality when using non-epitaxial growth substrates.

In this paper, we describe the design and fabrication of one proof-of-principle cell structure using TF-VLS grown p-InP absorber layers on Mo back contact substrates. The top window layer is an electron-selective titanium dioxide (TiO_2) film along with indium tin oxide (ITO) as the transparent conducting oxide. This forms a complete PV device stack of Mo/p-InP/n-TiO_2/ITO. The optoelectronic uniformity and effect of grain boundaries was examined by photoluminescence (PL) imaging and electron beam-induced current (EBIC) mapping. We also discuss the ex situ doping of these films from as-grown n-type to Zn-doped p-type. The first generation cells exhibit a power conversion efficiency of 12.1% under simulated 1 sun illumination with a V_{OC} of 692 mV. Furthermore, PL efficiency measurements show we have not reached the full optoelectronic potential of the material and higher device efficiency can be unlocked by improved device design.

2. Fabrication Scheme

The cell fabrication process shown in **Figure 1**a begins with growth of the InP absorber layer on either sputtered Mo (≈2 µm) on SiO_2/Si handling wafers or on Mo foil (50–500 µm). On top of the Mo, a 1–3 µm thick layer of In is evaporated.

This is then capped with a 30 nm layer of evaporated SiO_x. The entire stack is put into a tube furnace and heated in H_2 gas. Upon reaching the growth temperature of 750 °C, 10% phosphine (diluted in H_2) is introduced at 100 Torr for 10 min during which InP is grown. The thickness of the grown InP is ≈2× the initial In thin film. Following the growth, the InP is n-type due to donor-like native defects. The as-grown InP is then converted to p-type through a solid-source gas-phase diffusion process using either zinc or zinc phosphide in a sealed ampoule or a close spaced sublimation configuration. The doping is performed for 1 h at a sample temperature of 425 °C. Subsequently, the SiO_x cap is removed using a 1 min neat HF etch. Then a 15 nm n-TiO_2 window layer is deposited by atomic layer deposition using titanium isopropoxide and water precursors at a sample temperature of 120 °C. A 55 nm ITO layer is sputtered on top of the TiO_2 as the transparent electrode. Sputtering was done at room temperature at 0.9 mTorr Ar pressure with a resulting sheet resistance of ≈180 Ω sq⁻¹. The thickness of the combined TiO_2/ITO layers was optimized to minimize the reflectance, as described previously.[12] The ITO is then patterned by photolithography and etched using 1:3 HCl:H_2O into 1×1 mm² and smaller pads. Figure 1b shows a representative finished chip, where the darker regions are the patterned ITO. The TiO_2 layer is highly resistive and the p-InP minority carrier diffusion length is in the range of 1–3 µm (discussed below), thus allowing the ITO pad to effectively define the active cell area resulting in a relative error on the current density of less than 2%. A cross section scanning electron microscope (SEM) image of a completed cell on sputtered Mo is shown in Figure 1c, with a closer look at the front surface region shown in Figure 1d.
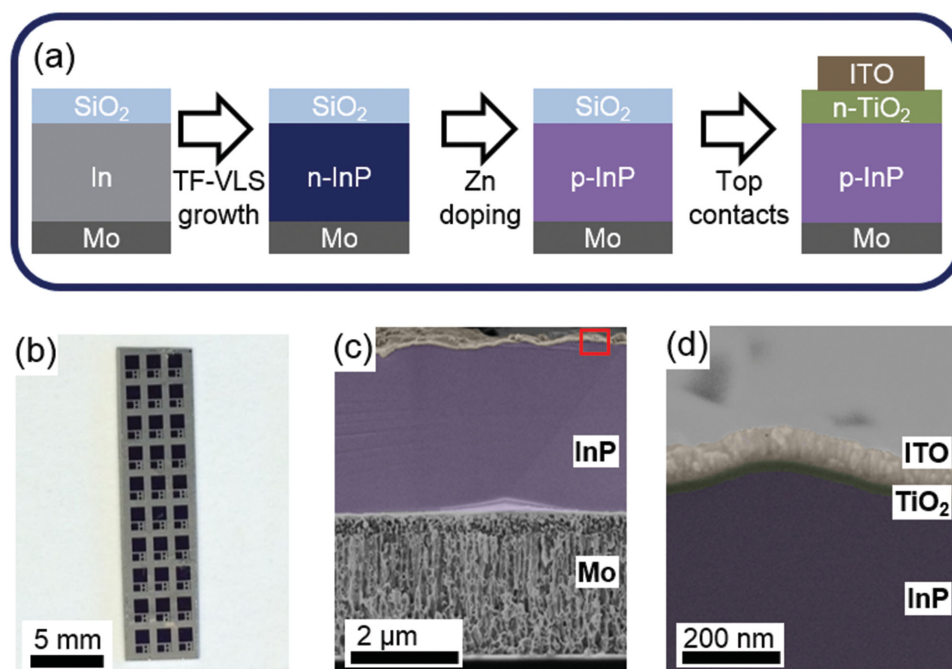

Figure 1. a) Schematic showing the cell fabrication process. b) Photograph of a completed chip with array of varying cell sizes. Dark areas are active cell regions. Cells are square with side lengths of 1 mm, 500 µm, 200 µm, and 100 µm. c) Cross section SEM image of a completed cell. d) Higher magnification cross section SEM image of the near surface region of a completed cell. SEM images are false colored.

www.MaterialsViews.com

ADVANCED
ENERGY
MATERIALS
www.advenergymat.de

FULL PAPER

3. Optoelectronic Structure of TF-VLS InP

The optoelectronic uniformity of the InP thin film was examined by large-area PL imaging. **Figure 2**a shows a top view optical microscope image of an as-grown *n*-InP layer. The surface roughness appears uniform overall with no features >1–2 μm. However in Figure 2b, the PL image over the same area reveals a dendritic microstructure. Earlier studies have shown that in TF-VLS growth each individual nuclei undergoes dendritic growth.[7,8] During the growth process, impurity segregation or accumulation of defects at the dendritic interfaces is believed to result in the observed contrast in luminescence. The PL intensity increases ≈7× from the dark extremities to the bright backbone of the dendrites in the area depicted. The PL images were acquired using a 635 nm LED as the excitation source, double-polished GaAs as the long-pass filter, and an Andor Luca R camera.

After full fabrication of the device, EBIC was used to extract electrical properties of the InP layer. An electron beam is scanned over a device, and the local current collected is mapped to reveal the presence of defects and junctions. EBIC is frequently used to extract the depletion width and the minority carrier diffusion length in solar cells.[13,14] Figure 2c,d shows a top view SEM image and the corresponding EBIC map over the same area, where darker regions correspond to a lower collection current. Here we used an accelerating voltage of 10 kV and a beam current of ≈100 pA. Monte Carlo simulations using CASINO were used to determine the penetration depth and generation volume.[15] We observe dark lines (lower current) that correspond to grain boundaries, as well as spatial variation in current collection within grains. The EBIC line profiles across a grain boundary were fit with a model (see the Supporting Information) to extract the local effective grain boundary recombination velocity (GBRV) and diffusion length (L_D).[16] The model assumes a geometry where the grain boundary is perpendicular to the junction, which is assumed to be the case here. It also assumes L_D is much greater than the depletion width (W_D), an assumption justified from capacitance–voltage (CV) measurements discussed below. From fitting several regions, L_D is determined to be 1 to 3 μm with an effective GBRV of 1×10^5 to 4×10^6 cm s^{-1}. These L_D values are confirmed from EBIC scans using an alternative geometry (the Supporting Information). Similarly doped single crystal *p*-InP has L_D of 1 to 40 μm and an effective surface recombination velocity (SRV) of ≈10^5 cm s^{-1}, comparable to our values.[17,18] Compared to the diffusion length in state-of-the-art CdTe (1 to 8 μm) and CIGS (0.5 to >2 μm),[19,20] L_D values from TF-VLS InP are similar. The effective GBRV values are higher than the reported values
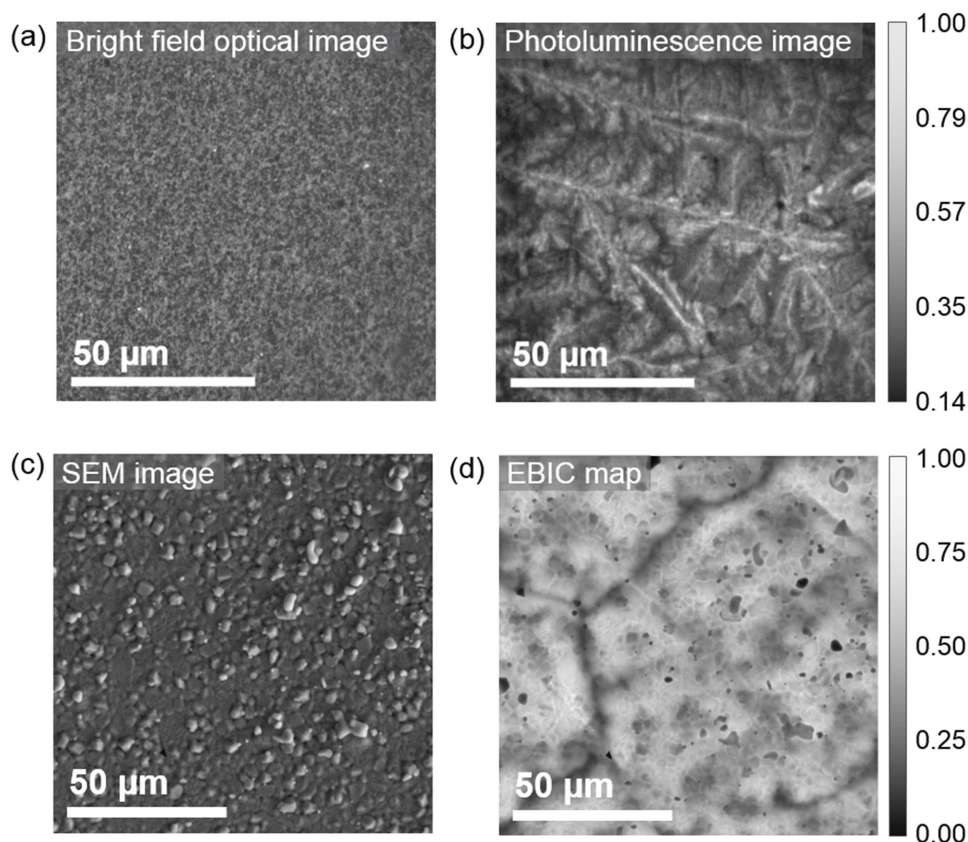

Figure 2. a,b) Bright field optical and PL images from the same area for an as-grown n-InP sample. The surface roughness looks very uniform, but PL reveals a dendritic optoelectronic structure that mirrors known growth patterns. c,d) SEM and EBIC images from the same area (but different from (a) and (b)) of a Zn-doped device. Again the surface roughness is uniform but variation in the underlying optoelectronic structure is visible. Grain boundaries are visible as dark lines and some surface occlusions can be seen. Intensity scale bars are in arbitrary units and normalized to the maximum intensity.

**ADVANCED
ENERGY
MATERIALS**

www.advenergymat.de

www.MaterialsViews.com

Makrials Views

FULL PAPER

for CdTe and CIGS, which are both <10^3 cm s^{-1}.[21,22] Impurity segregation at grain boundaries during the growth or doping stages may account for these differences. Additionally, the close proximity of the rear Mo contact can negatively affect the minority carrier recombination and thus the apparent diffusion length. However, due to the larger lateral grain sizes in TF-VLS InP compared to CIGS and CdTe,[7] there is a proportionately smaller density of grain boundaries and so they should have a smaller effect on device performance.

4. Ex Situ Zn Doping

The ex situ Zn *p*-doping process used for TF-VLS InP was examined in detail. As an acceptor, Zn occupies substitutional indium sites,[23] and is known in the literature to be a fast diffuser in InP with a substitutional-interstitial diffusion mechanism.[24–26] However, the diffusion coefficient at a given temperature also depends on the Zn concentration,[25,26] phosphorous pressure,[25] and background donor concentration,[24] factors which all affect the vacancy concentration in the lattice. The hole concentration from Zn doped InP is reported to saturate at ($\approx$1.5–5) $\times$ 10^{18} cm^{-3}, where compensating donors and precipitates form.[23,27–29] To obtain uniform doping in our TF-VLS InP, we chose a temperature and time regime that yields a Zn diffusion length greater than the InP thickness. At 450 °C for 1 hour, the expected diffusion length is $\approx$4–5 μm,[24–26,30] exceeding the InP thickness, but may be even higher due to the polycrystalline nature of our film. At temperatures lower than 400 °C, type conversion is not reliable, and at temperatures higher than 450 °C, significant thermal decomposition occurs. The presence of phosphorus in the doping source helps prevent InP surface decomposition.

CV measurements of completed devices were carried out to determine the depletion width and net hole concentration near the surface after doping. 100 nm thick Au was deposited on top of the ITO to reduce series resistance. The net hole concentration vs. depth is extracted from the slope of the $1/C^2$ curve using the Mott–Schottky equations with the assumption of a one-sided junction.[31,32] Representative data are shown in **Figure 3**a. The net hole concentration is relatively constant along the probed depth, and is between 3 $\times$ 10^{16} and 3 $\times$ 10^{17} cm^{-3} for different samples using the same doping conditions, corresponding to depletion widths of $\approx$75 to 130 nm. Secondary ion mass spectroscopy (SIMS) analysis was then used to measure the Zn concentration as a function of depth (Figure 3b). At the front surface the concentration is $\approx$5 $\times$ 10^{18} cm^{-3}. The concentration of Zn is larger than the hole concentration near the surface, implying a dopant activation of $\approx$10%. We observe Zn segregation at the back InP-Mo interface with a back surface Zn concentration of $\approx$2 $\times$ 10^{20} cm^{-3}. After doping, the Mo back contact also has a low contact resistance of <0.05 Ω cm^2 to *p*-type InP, measured using test structures. This effect may result from Zn segregation at the back interface creating a *p*++ region or alloy.

To characterize defect state formation, low-temperature PL was performed at different stages of the doping process (Figure 3c): as-grown *n*-InP sample ($n \approx 8 \times 10^{16}$ cm^{-3}), a partially compensated Zn doped sample ($n \approx 2 \times 10^{15}$ cm^{-3}), and

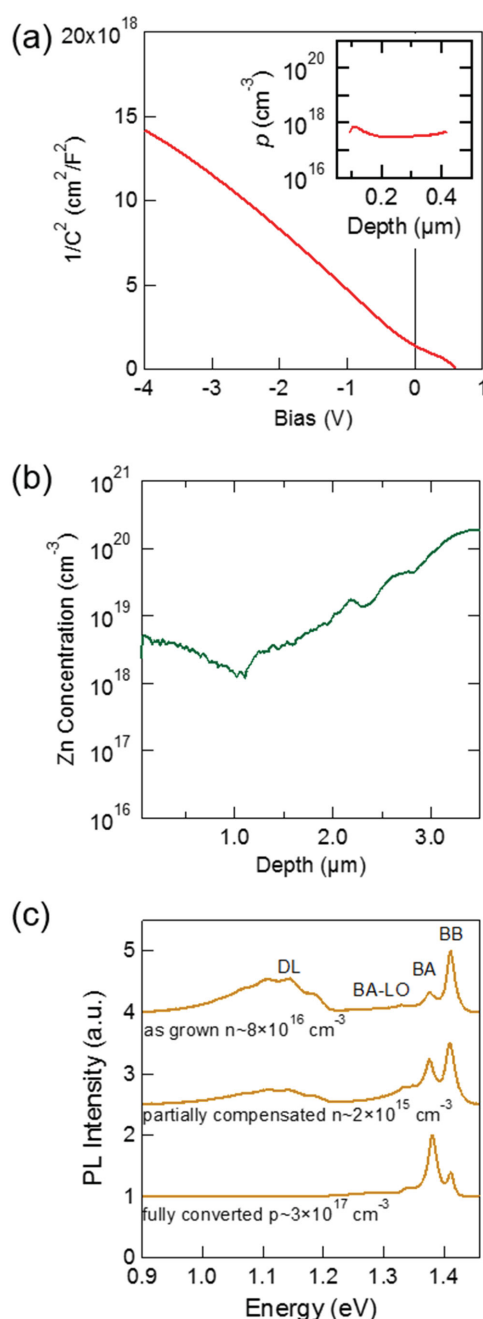**Figure 3.** a) Representative 1/capacitance^2-voltage measurement of a completed device. Inset shows the extracted hole concentration as a function of depth. b) SIMS depth profile of Zn concentration. c) PL spectra taken at 8 K. Top curve is from an as-grown sample ($n \approx 8 \times 10^{16}$ cm^{-3}), middle curve is from partially compensated sample ($n \approx 2 \times 10^{15}$ cm^{-3}), bottom curve is fully converted to p-type ($p \approx 3 \times 10^{17}$ cm^{-3}). Peak assignments are discussed in the text.

a fully converted Zn doped sample ($p \approx 3 \times 10^{17}$ cm^{-3}). Here the carrier concentrations correspond to the surface values extracted from Mott–Schottky measurements The measurement temperature was 8 K and the excitation source was the 488 nm line from an Ar ion laser. From the literature, we can identify the peaks from high to low energy as the band-to-band (BB)

transition at 1.411 eV, the Zn band-to-acceptor (BA) transition at 1.376 eV, a small LO phonon replica of the BA transition (BA-LO) at 1.333 eV, and a broad peak relating to several deep levels (DL) below 1.2 eV.[33–36] In the partially compensated sample, the BA peak becomes stronger compared to the BB peak, and the intensity of the DL peaks decreases. These trends continue in the fully converted sample. The increase of the BA to BB peak intensity ratio in our samples is attributed to increased Zn doping. DL peaks do not appear in reference S-doped n-InP and Zn-doped p-InP wafers with similar concentrations. In the literature these peaks are associated with transition metal impurities and phosphorus vacancies.[37–39] In our samples out-diffusion of metal impurities from the Mo substrate (99.95% purity) during the InP growth process is a potential explanation for the appearance of DL peaks, and their disappearance may be a result of Zn compensation or annealing out of those states during doping.

5. Solar Cell Performance and Characterization

Following the doping study, we evaluated the solar cell performance of the completed devices. The band diagram under equilibrium is presented in **Figure 4**a, which illustrates the electron selective behavior of the p-InP/n-TiO$_2$ heterojunction, using $p = 3 \times 10^{17}$ cm^{-3} in InP, $n = 7 \times 10^{16}$ cm^{-3} in TiO$_2$, and previously reported band alignments.[12] Electrically, the n-TiO$_2$ layer acts as an electron selective contact, due to its band alignment with p-InP.[12] TiO$_2$ has a band gap of 3.4 eV and its conduction band is well aligned with that of InP. On the other hand, there is a large valence band offset of ≈2 eV between InP and TiO2. Electrons can drift freely from InP into TiO$_2$, but holes are blocked by the band bending and the large valence band offset. Figure 4b shows the dark and illuminated current density versus voltage (J–V) for a 0.5 × 0.5 mm^2 cell. Due to the size of the cell, there is some uncertainty to the J_{SC} measurements due to possible edge effects.[40] Specifically, a probe tip was used to directly contact the ITO pads at the corners, causing shadowing of ≈9% of the active area. From an EBIC line scan (Supporting Information) current collection did not extend past ≈2–3 μm beyond the edge of the ITO pads, which leads to a ≈2% relative error in the current density. A Solar Light 16S 300W solar simulator was used as the light source at 1 sun intensity (100 mW cm^{-2}, AM1.5G) at 25 °C. This cell had the highest power conversion efficiency of 12.1%. The cell exhibits a V_{OC} of 692 mV, short-circuit current density (J_{SC}) of 26.9 mA cm^{-2} (not corrected for shadowing), and fill factor (FF) of 65%. In comparison, to reach the InP Shockley–Queisser (SQ) limit of ≈33.5% efficiency at 1 sun AM1.5G requires a V_{OC} of ≈1.08 V, J_{SC} of ≈34.9 mA cm^{-2}, and FF of ≈89%.[41,42] Series and shunt resistances of 1.5 and 1616 Ω cm^2 were extracted by fitting the curve around open-circuit and past short-circuit. Parasitic resistances strongly limit the performance of this cell. The series resistance is due in part to the sheet resistance of the ITO layer, the thickness of which was primarily optimized for minimizing reflection. ITO contributes >0.3 Ω cm^2 to the series resistance in our measurement geometry.[43] The low shunt resistance may be caused by small pinholes in the InP film or conduction paths through grain boundaries; further study is needed. The reflection (1-R) and external quantum efficiency
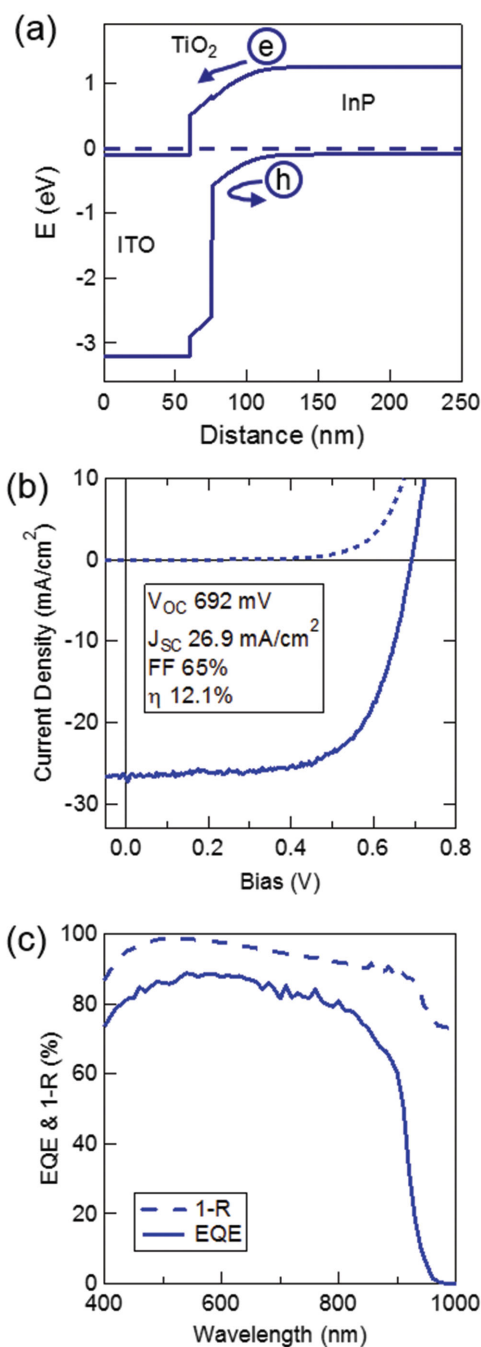

Figure 4. a) Calculated equilibrium band diagram of the top surface region of the device. b) J–V measurements for a cell under simulated 1 sun illumination (solid line) and in the dark (dotted line). Device parameters were V_{OC} of 692 mV, J_{SC} of 26.9 mA cm^{-2}, FF of 65%, and power conversion efficiency of 12.1%. Cell area was 0.5 × 0.5 mm^2. c) Corresponding EQE and 1-R curves.

(EQE) of the cell is plotted in Figure 4c. Extracting the current from the EQE gives ≈28 mA cm^{-2}, close to the measured J_{SC} value. The current loss due to reflection is ≈2.6 mA cm^{-2}. The step in the 1-R curve at the band edge of InP around 925 nm is from sub-band gap light passing through the InP layer and reflecting from the Mo back contact. This shows that although
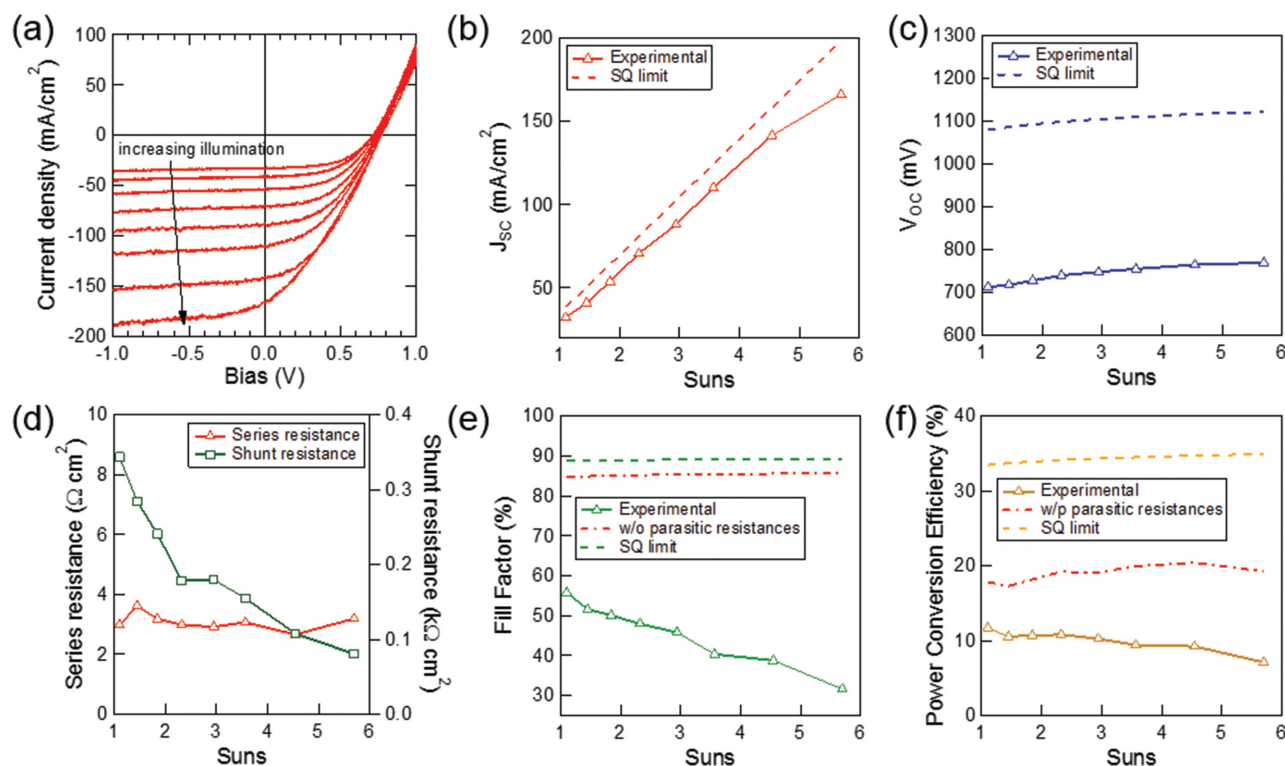
ADVANCED
ENERGY
MATERIALS
www.advenergymat.de

www.MaterialsViews.com

FULL PAPER

Figure 5. a) J–V measurements of a cell under simulated 1.1 to 5.7 suns illumination intensity. Cell area is 1 mm². b) J_{SC} versus illumination intensity. (c) V_{OC} vs. illumination intensity. (d) Extracted series and shunt resistances from J–V curves. e) FF versus illumination intensity. Potential fill factor without parasitic series and shunt resistances is additionally shown as dotted-dashed red line. f) Power conversion efficiency versus illumination intensity. Red dotted-dashed line shows projected efficiency without parasitic resistances. Experimental and SQ limit values for InP solar cell parameters are shown as solid lines with markers and dashed lines, respectively. Markers indicate measured data points and connecting lines are used as guides for the eye.

the reflectivity of Mo is not high,[44] it may still enhance the current collection in the near infrared region where the absorption length (≈1.3 µm at 921 nm)[45] is comparable to the film thickness. The EQE itself has a near constant offset from the 1-R until ≈850 nm, with the difference due to parasitic absorption or recombination losses.

The J–V of a representative cell (1 × 1 mm²) was measured at illumination intensities from 1.1 to 5.7 suns (**Figure 5**a), and compared to the theoretical ideal cases to examine sources of loss. Measurement temperatures were maintained in the range 27.6–28.6 °C, leading to ≈2 mV variation in V_{OC} and negligible impact on other parameters.[46] The J_{SC} dependence on the illumination intensity is close to ideal, as shown in Figure 5b. J_{SC} linearly increases with illumination intensity up to 4.5 suns, beyond which the series resistance begins to limit J_{SC}. The average J_{SC} (not correcting for shadowing by probe tip) is ≈85% of the theoretical maximum, with ≈8% loss due to reflection and the remainder due to probe shadowing, parasitic absorption in the window layers, and bulk and surface recombination. In Figure 5c, the V_{OC} increases logarithmically with illumination intensity, as expected. The ideality factor extracted from the J_{SC}–V_{OC} curve is ≈1.41, close to the value extracted by luminescence efficiency measurements discussed in detail below. An ideality factor ≥1 is indicative of non-radiative recombination, which reduces V_{OC} from the theoretical limit.

The FF loss due to parasitic resistances is a major cause of lower efficiency in this device (Figure 5d,e). In an ideal cell,

the FF is expected to change only slightly with illumination intensity. In the measured cell, the parasitic series resistance is ≈3 Ω cm² and the parasitic shunt resistance is 81 to 343 Ω cm², which were extracted from the J–V curves near open-circuit and past short-circuit. The FF values of 31% to 55% are compared to the ideal case without parasitic resistances, which is plotted in Figure 5e. In the ideal case, FF is determined by the V_{OC} and the ideality factor. With an ideality factor of 1 and the measured V_{OC} values, the FF would be ≈85%. Also shown is the theoretical FF of ≈89% for this band gap in the SQ limit.[42] The measured power conversion efficiencies as a function of illumination intensity are plotted in Figure 5f, which range from 7.1% (5.7 suns) to 11.7% (1.1 sun). We compare these efficiencies to the projected case without parasitic resistances, also shown in Figure 5f. These projected efficiencies use the measured J_{SC} and V_{OC} values, but FF with parasitic resistances removed and ideality factor of 1. In this scenario the efficiencies reach 17.3% (1.1 sun) to 20.4% (4.5 suns). While it is unrealistic to assume parasitics can be fully removed, this provides a guide for future development.

6. External Luminescence Efficiency and Future Potential

To further study the future potential of InP thin film devices grown by the TF-VLS method we measured the external
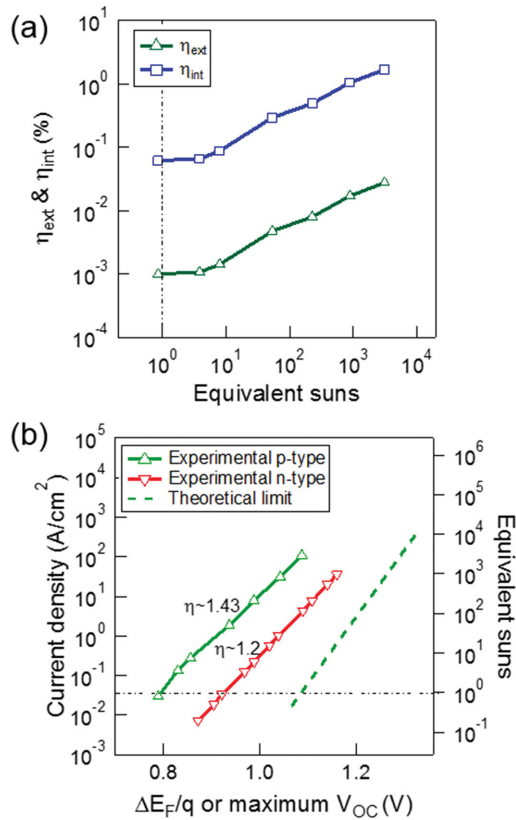
www.MaterialsViews.com

ADVANCED
ENERGY
MATERIALS
www.advenergymat.de

FULL PAPER

Figure 6. a) External (η_{ext}) and internal (η_{int}) luminescence efficiency versus illumination intensity from p-type TF-VLS InP. 1 equivalent sun illumination gives the same photon flux as a 1 sun AM1.5G source when using monochromatic 514 nm light instead. b) The optical "J–V" curve corresponding to the η_{ext} in a) is shown in green. Our previously published "J–V" curve for n-type InP is reproduced as well in red for comparison. Dashed line shows the theoretical limit for InP.

luminescence efficiency (η_{ext}), defined as the number of photons emitted per photon absorbed. From η_{ext} we extracted the internal luminescence efficiency (η_{int}), defined as the radiative recombination rate divided by the total recombination rate.[47] In a perfect material η_{int} is 100%. This means radiative recombination is the only carrier recombination mechanism, a necessary condition to reach the SQ limit. In addition, η_{ext} is directly related to the quasi-Fermi level splitting (ΔE_F) or maximum possible V_{OC} through Equation (1)[48]

$$\Delta E_F = kT \ln\left(\frac{R_{abs}}{R_{em}}\right) + kT \ln\left(\eta_{ext}\right) \qquad (1)$$

$$R_{em} = \pi \int_{E_g}^{\infty} \frac{2n_r^2}{h^3 c^2} \frac{E^2}{e^{E/kT}-1}\, dE \qquad (2)$$

where R_{abs} is the absorbed photon flux, R_{em} is the emitted black body photon flux at thermal equilibrium, n_r is the refractive index of air, k is the Boltzmann constant, T is the temperature, E is the photon energy, c is the speed of light, h is the Planck constant, and E_g is the band gap. Absorbance is assumed to be an angle-independent step function at the band gap and the

factor of π arises from the assumption of Lambertian emission. The second term in the ΔE_F equation is the voltage loss due to $\eta_{ext} < 100\%$. Thus, η_{ext} is a measurement of the maximum V_{OC} achievable in the material, unconstrained by parasitic absorption or contact losses.[48] **Figure 6**a shows measured η_{ext} and extracted η_{int} for different excitation intensities. The excitation source used was a 514 nm Ar ion laser, with intensities from 72×10^6 to 1.55×10^6 mW cm^{-2}. The corresponding photon fluxes were converted to equivalent current densities ($J = q \times$ flux) or AM1.5G equivalent suns. With a band gap of 1.344 eV, the total above band gap photon flux under 1 sun AM1.5G illumination is $\approx 2.2 \times 10^{17}$ cm^{-2} s^{-1} for InP. This photon flux corresponds to an absorbed power density of ≈ 84 mW cm^{-2} for monochromatic 514 nm illumination, which we call 1 sun equivalent.

Figure 6b shows the optical "J–V" curve in green corresponding to the measured η_{ext} in Figure 6a. To understand the shape of the curve, we model it with the equation[47]

$$J \propto An + Bnp + C\left(np^2 + pn^2\right) \qquad (3)$$

where A, B, and C are the Shockley–Read–Hall (SRH), radiative, and Auger recombination coefficients, respectively. n and p are the electron and hole concentrations. Under low level injection, where the excess electron concentration (Δn) is much less than the background acceptor concentration (N_A), n and p are related to ΔE_F by[31]

$$n \cong \Delta n = \frac{n_i^2}{N_A} \exp(\Delta E_F/kT) \qquad (4)$$

$$p \cong N_A \qquad (5)$$

Under high level injection, where Δn is greater than N_A, the relations become

$$n \cong \Delta n = n_i \exp(\Delta E_F/2kT) \qquad (6)$$

$$p \cong \Delta n \qquad (7)$$

where n_i is the intrinsic carrier concentration, k is the Boltzmann constant, and T is the temperature. If we then assume one recombination mechanism dominates, J is approximated as

$$J \cong J_0 \exp\left(\Delta E_F / \eta kT\right) \qquad (8)$$

where η is the ideality factor. This ideality factor depends on the injection level as well as the dominant recombination mechanism. In low level injection, $\eta = 1$ for all three recombination mechanisms. However, in high level injection, SRH recombination gives $\eta = 2$, radiative recombination gives $\eta = 1$, and Auger recombination gives $\eta = 2/3$.[47] There are two factors this simple model does not include. The first is the exponentially decaying generation rate with depth that will produce a corresponding depth dependent injection level, and the second is the effect of a depletion region at the top surface. Both of these can lead to situations with simultaneous high level and low level injection resulting in η between 1 and 2. In Figure 6b,

FULL PAPER

we fit $\eta \approx 1.43$ for the optically implied "J–V" of our TF-VLS p-InP, and extract a $\Delta E_F/q$ of ≈795 mV. While this indicates SRH recombination is present in our material, it is still higher than the electrically achieved V_{OC} of 692 mV and indicates there is room to improve in the optical and contact design of the device.

Next, we discuss sources of loss contributing to the difference in $\Delta E_F/q$ of bare material and electrical V_{OC} of finished devices. The luminescence efficiency measurement on bare InP samples takes into account recombination losses at the free top surface, in the bulk, and at the back Mo interface. The combined effect of these determines ΔE_F. After configuring the InP into a device, additional sources of loss are introduced which lower ΔE_F directly. The interface between the TiO$_2$ and InP, being nonepitaxial, can have a large defect density that causes increased nonradiative recombination. Another effect is that the band bending formed by the junction causes drift of minority carriers to the front surface where they recombine, resulting in a larger SRV than at a bare surface. Other factors produce a difference between $\Delta E_F/q$ and V_{OC} of finished devices, such as work function mismatches between the top ITO-TiO$_2$ contact and back Mo-InP contact, or low built-in potential due to low TiO$_2$ doping (≈7 × 10^{16} cm^{-3}). Finally, spatial variation in the luminescence efficiency (which can be seen in Figure 2b) also contributes to this difference. The ≈7× spatial variation of PL intensity translates to ≈50 meV variation in local ΔE_F, but the variation may be greater over larger areas. This effect could be modeled with band tails to explain lower V_{OC}, as recently studied in CZTS.[49]

For comparison, our previously reported "J–V" curve for as-grown n-InP is reproduced in Figure 6b with $\eta \approx 1.2$ and ΔE_F of ≈930 mV at 1 sun illumination.[7] The theoretical limit for InP is also plotted as a dashed line for comparison. It is well known that n-type InP has much higher lifetimes than comparably doped p-type InP and thus the potential to reach a higher V_{OC} and efficiency.[50] However, the lack of a suitable, non-epitaxial hole selective window layer has limited the device design options. This is the area of active research and will open up new possibilities in the future for using n-type InP as the absorber layer for higher performance.[51] A cell with V_{OC} of 930 mV has the potential to reach 24.1% power conversion efficiency assuming an achievable J_{SC} of 32 mA cm^{-2} and fill factor of 81%.

7. Conclusion

In conclusion, we have introduced a new thin-film InP solar cell design, where large-grain InP is grown directly on a non-epitaxial Mo substrate using the TF-VLS method. We considered film morphology and uniformity, electrical behavior of grain boundaries, and effects of an ex situ Zn doping process. The highest power conversion efficiency achieved under simulated 1 sun illumination is 12.1%, with V_{OC} of 692 mV, J_{SC} of 26.9 mA cm^{-2}, and FF of 65%. The highest measured V_{OC} is 692 mV at ≈1 sun, while luminescence efficiency measurements indicate a potential V_{OC} of ≈795 mV. The results presented here represent a promising starting point for further development of large-scale terrestrial III–V photovoltaics.

Supporting Information

Supporting Information is available from the Wiley Online Library or from the author.

[1] M. A. Green, K. Emery, Y. Hishikawa, W. Warta, E. D. Dunlop, *Prog. Photovoltaics Res. Appl.* **2015**, *23*, 1.

[2] M. Woodhouse, A. Goodrich, *Manufacturing Cost Analysis Relevant to Single-and Dual-Junction Photovoltaic Cells Fabricated with III-Vs and III-Vs Grown on Czochralski Silicon* **2014**.

[3] M. Bosi, C. Pelosi, *Prog. Photovoltaics Res. Appl.* **2007**, *15*, 51.

[4] B. M. Kayes, H. Nie, R. Twist, S. G. Spruytte, F. Reinhardt, I. C. Kizilyalli, G. S. Higashi, in *37th IEEE Photovoltaics Spec. Conf. (PVSC), 37th*, IEEE, Seattle, WA, **2011**, p. 000004.

[5] L. S. Mattos, S. R. Scully, M. Syfu, E. Olson, L. Yang, C. Ling, B. M. Kayes, G. He, IEEE, Austin, TX, in *IEEE Photovoltaics Spec. Conf. (PVSC), 38th*, **2012**, p. 003187.

[6] W. Shockley, H. J. Queisser, *J. Appl. Phys.* **1961**, *32*, 510.

[7] R. Kapadia, Z. Yu, H.-H. H. Wang, M. Zheng, C. Battaglia, M. Hettick, D. Kiriya, K. Takei, P. Lobaccaro, J. W. Beeman, J. W. Ager, R. Maboudian, D. C. Chrzan, A. Javey, *Sci. Rep.* **2013**, *3*, 2275.

[8] R. Kapadia, Z. Yu, M. Hettick, J. Xu, M. S. Zheng, C.-Y. Chen, A. D. Balan, D. C. Chrzan, A. Javey, *Chem. Mater.* **2014**, *26*, 1340.

[9] R. S. Wagner, W. C. Ellis, *Appl. Phys. Lett.* **1964**, *4*, 89.

[10] T. J. Trentler, K. M. Hickman, S. C. Goel, A. M. Viano, P. C. Gibbons, W. E. Buhro, *Science* **1995**, *270*, 1791.

[11] X. Duan, C. M. Lieber, *Adv. Mater.* **2000**, *12*, 298.

[12] X. Yin, C. Battaglia, Y. Lin, K. Chen, M. Hettick, M. Zheng, C.-Y. Chen, D. Kiriya, A. Javey, *ACS Photonics* **2014**, *1*, 1245.

[13] H. J. Leamy, *J. Appl. Phys.* **1982**, *53*, R51.

[14] O. Kurniawan, V. K. S. Ong, *IEEE Trans. Electron Devices* **2006**, *53*, 2358.

[15] D. Drouin, A. R. Couture, D. Joly, X. Tastet, V. Aimez, R. Gauvin, *Scanning* **2007**, *29*, 92.

[16] A. Romanowski, A. Buczkowski, *Solid State Electron.* **1985**, *28*, 645.

[17] C. A. Hoffman, H. J. Gerritsen, A. V. Nurmikko, *J. Appl. Phys.* **1980**, *51*, 1603.

[18] C. A. Hoffman, K. Jarašiūnas, H. J. Gerritsen, A. V. Nurmikko, *Appl. Phys. Lett.* **1978**, *33*, 536.

[19] G. Brown, V. Faifer, A. Pudov, S. Anikeev, E. Bykov, M. Contreras, J. Wu, *Appl. Phys. Lett.* **2010**, *96*, 022104.

[20] A. Morales-Acevedo, *Solar Energy* **2006**, *80*, 675.

[21] B. G. Mendis, L. Bowen, Q. Z. Jiang, *Appl. Phys. Lett.* **2010**, *97*, 092112.

[22] W. K. Metzger, I. L. Repins, M. Romero, P. Dippo, M. Contreras, R. Noufi, D. Levi, *Thin Solid Films* **2009**, *517*, 2360.

[23] R. S. Williams, P. A. Barnes, L. C. Feldman, *Appl. Phys. Lett.* **1980**, *36*, 760.

[24] G. J. van Gurp, P. R. Boudewijn, M. N. C. Kempeners, D. L. A. Tjaden, *J. Appl. Phys.* **1987**, *61*, 1846.

[25] B. Tuck, A. Hooper, *J. Phys. D: Appl. Phys* **1975**, *8*, 1806.

[26] L. L. Chang, H. C. Casey Jr., *Solid State Electron.* **1964**, *7*, 481.

[27] A. W. Nelson, L. D. WestBrook, *J. Cryst. Growth* **1984**, *68*, 102.

[28] K. M. Yu, W. Walukiewicz, L. Y. Chan, R. Leon, E. E. Haller, J. M. Jaklevic, C. M. Hanson, *J. Appl. Phys.* **1993**, *74*, 86.

[29] L. Y. Chan, K. M. Yu, M. Ben-Tzur, E. E. Haller, J. M. Jaklevic, W. Walukiewicz, C. M. Hanson, *J. Appl. Phys.* **1991**, *69*, 2998.

[30] H. S. Marek, H. B. Serreze, *Appl. Phys. Lett.* **1987**, *51*, 2031.

[31] S. M. Sze, K. K. Ng, *Physics of Semiconductor Devices*, John Wiley & Sons, Hoboken, NJ, **2006**.

[32] J. D. Plummer, M. Deal, P. D. Griffin, *Silicon VLSI Technology: Fundamentals, Practice, and Modeling*, 1st ed., Prentice Hall, Upper Saddle River, NJ **2000**.

[33] S. Banerjee, A. K. Srivastava, B. M. Arora, *J. Appl. Phys.* **1990**, *68*, 2324.

[34] J. Chevrier, A. Huber, N. T. Linh, *J. Appl. Phys.* **1980**, *51*, 815.

[35] E. Kubota, Y. Ohmori, K. Sugii, *J. Appl. Phys.* **1984**, *55*, 3779.

[36] Y. Moon, S. Si, E. Yoon, S. J. Kim, *J. Appl. Phys.* **1998**, *83*, 2261.

[37] M. S. Skolnick, E. J. Foulkes, B. Tuck, *J. Appl. Phys.* **1984**, *55*, 2951.

[38] H. Temkin, B. V. Dutt, W. A. Bonner, *Appl. Phys. Lett.* **1981**, *38*, 431.

[39] H. Temkin, B. V. Dutt, W. A. Bonner, V. G. Keramidas, *J. Appl. Phys.* **1982**, *53*, 7526.

[40] C. R. Osterwald, K. A. Emery, *Solar Cells* **1983**, *10*, 1.

[41] C. H. Henry, *J. Appl. Phys.* **1980**, *51*, 4494.

[42] M. A. Green, *Solid State Electron.* **1981**, *24*, 788.

[43] U. Malm, M. Edoff, *Prog. Photovoltaics Res. Appl.* **2008**, *16*, 113.

[44] B. W. Veal, A. P. Paulikas, *Phys. Rev. B* **1974**, *10*, 1280.

[45] O. J. Glembocki, H. Piller, in *Handbook of Optical Constants of Solids*, (Ed: E. D. Palik), Academic Press, Burlington **1997**, p. 503.

[46] P. Singh, N. M. Ravindra, *Sol. Energy Mater. Sol. Cells* **2012**, *101*, 36.

[47] S. L. Chuang, *Physics of Photonic Devices*, 2 ed., Wiley, Hoboken, NJ **2012**.

[48] O. D. Miller, E. Yablonovitch, S. R. Kurtz, *IEEE J. Photovoltaics* **2012**, *2*, 303.

[49] T. Gershon, B. Shin, N. Bojarczuk, T. Gokmen, S. Lu, S. Guha, *J. Appl. Phys.* **2013**, *114*, 154905.

[50] Y. Rosenwaks, Y. Shapira, D. Huppert, *Phys. Rev. B* **1991**, *44*, 13097.

[51] G. Hautier, A. Miglio, G. Ceder, G.-M. Rignanese, X. Gonze, *Nat. Commun.* **2013**, *4*, 2292.